CARBON 62 (2013) 182–192

Available at www.sciencedirect.com

SciVerse ScienceDirect

journal homepage: www.elsevier.com/locate/carbon

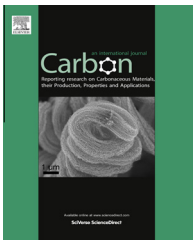

Ag-stabilized few-layer graphene dispersions in low boiling point solvents for versatile nonlinear optical applications

Zhenyu Sun [a], *Ningning Dong* [b], *Kangpeng Wang* [b], *Dennis König* [c], *Tharamani Chikka Nagaiah* [d], *Miguel D. Sánchez* [a,e], *Alfred Ludwig* [c], *Xin Cheng* [b], *Wolfgang Schuhmann* [d], *Jun Wang* [b,*], *Martin Muhler* [a,*]

[a] *Laboratory of Industrial Chemistry, Ruhr-University Bochum, D-44780 Bochum, Germany*

[b] *Key Laboratory of Materials for High-Power Laser, Shanghai Institute of Optics and Fine Mechanics, Chinese Academy of Sciences, Shanghai 201800, China*

[c] *Department of Mechanical Engineering, Institute for Materials, Ruhr-University Bochum, D-44780 Bochum, Germany*

[d] *Analytische Chemie-Elektroanalytik & Sensorik, Ruhr-University Bochum, D-44780 Bochum, Germany*

[e] *Departamento de Física and Instituto de Física del Sur, Universidad Nacional del Sur-CONICET, 8000 Bahía Blanca, Argentina*

ARTICLE INFO

Article history:
Received 4 March 2013
Accepted 4 June 2013
Available online 11 June 2013

ABSTRACT

A solution stabilization strategy that uses an easily removable media is critical to graphene (G) applications. Here, we demonstrate that highly stable graphene dispersions in low boiling point solvents such as isopropanol can be readily achieved by the uniform deposition of Ag nanoparticles (NPs) on the surface of graphene. Optimizing the synthesis parameters such as ultrasonic intensity, feeding strategy, loading content and precursor concentration allowed us to tune the particle size and, in this way, the stabilizing effects of the NPs on the dispersions. The as-obtained Ag/G/i-PrOH dispersions exhibit versatile nonlinear optical properties suggesting a great potential in nanophotonic applications such as absorber for ultrafast lasers and eye protection.

1. Introduction

Two-dimensional atomic crystals were argued to be thermodynamically unstable and presumed not to exist until 2004 when graphene (G) was first experimentally isolated by a delicate handcraft (scotch-tape technique) [1]. Research on graphene has developed at a very rapid pace because of its extremely high carrier mobility, mechanical flexibility, optical transparency, and chemical stability, among others [2–5]. For many applications, producing pristine graphene sheets in large quantities is a prerequisite. This can be achieved by exfoliation of graphene from natural graphite in the liquid phase [6–11]. In addition to its low cost, simplicity and high scalability, the method also allows for flexible manipulation of graphene into various processes, such as impregnation, blending, casting, or functionalization. High-quality dispersions of graphene without oxidation have been obtained by using such solvents with Hansen solubility parameters that matched reasonably well with those suggested for graphene [6–10]. However, the best solvents mostly have high boiling points leading to removal problems during processing. Similar challenges also occur for surfactant- or polymer-exfoliated graphene. Additionally, aggregation would take place during the slow solvent evaporation making it difficult to deposit

* *Corresponding authors:* Fax: +49 234 3214115.
E-mail addresses: jwang@siom.ac.cn (J. Wang), muhler@techem.rub.de (M. Muhler).
0008-6223/$ - see front matter
http://dx.doi.org/10.1016/j.carbon.2013.06.010

individual graphene sheets from the dispersion. To address these issues, exfoliating graphene in solvents with low boiling temperatures appears promising, although the graphene dispersions in such solvents are relatively unstable. Correspondingly, it is of great significance to develop an effective strategy to enhance the stability of the system to foster practical applications.

Graphene has recently been demonstrated as a promising candidate material for photonic and optoelectronic nanodevices [12–16]. Single-layer graphene absorbs approximately 2.3% of incident white light [5], and possesses a very high absorption coefficient of up to 3.01×10^5 cm^{-1}, being 70 times larger that of GaAs [17]. In contrast to C_{60} that only has a nonlinear optical (NLO) response in the visible spectral region, pristine graphene dispersions exhibit ultrafast carrier relaxation times and broadband NLO responses to nanosecond pulses from the visible to the near infrared regime [12]. The principle mechanism for such NLO response is nonlinear scattering that arises from the formations of solvent bubbles and microplasmas [12]. Alternatively, tailoring the electronic bandgap of graphene by chemical doping, applied bias, and adsorption of gases and water molecules offers a tunable platform for optical applications. The unique two-dimensional sp^2 carbon network of graphene also permits formation of versatile NLO hybrid structures by attaching functional materials, such as metal nanoparticles (NPs) or polymers [16]. So far, most previous work in this regard employs graphene oxide or reduced graphene oxide as a support [18,19], the properties of which differ significantly from those of pristine graphene. Therefore, it is interesting to explore the NLO properties of pure graphene-based composites.

Here, we demonstrate that the deposition of Ag NPs on graphene surfaces is capable of effectively enhancing the stability of graphene dispersions in low boiling point solvents (isopropanol (i-PrOH), acetone). The obtained Ag-stabilized graphene dispersions were used for the preparation of conductive films. Applying high-intensity ultrasound during the synthetic procedure facilitated rapid occurrence of primary nucleation, and as a result, small crystals with uniform size were formed and homogeneously deposited onto graphene. Note that no capping ligands are required during the process, resulting in clean surfaces for the NPs and avoiding the problem that the stabilizer molecules adversely affect particle properties. The size of the NPs can be readily tuned by controlling their degree of loading on graphene, ultrasonic intensity, precursor concentration, and feeding strategy. Such a scenario allows us to investigate the stability of graphene dispersions in relation to the size and loading content of Ag NPs, as well as the NLO response of the resulting Ag-graphene composites. Moreover, the NLO mechanism of the composites is discussed.

2. Experimental

2.1. Materials

All chemicals used in this work were of analytical grade and used as supplied. Isopropanol (product number 20842.312) was supplied by VWR International. Acetone (product number 1205409002) was obtained from Avantor Performance Materials. Graphite powder (product number 332461) and $AgNO_3$ (product number 209139) were both provided by Sigma–Aldrich and used without further treatments. $NaBH_4$ (product number 8.06373.0100) was obtained from Merck Schuchardt OHG.

2.2. Dispersion of graphene in low boiling point solvents

Graphene dispersions were prepared by adding graphite at an initial graphite concentration of 5 mg mL^{-1} to 400 mL solvent (i-PrOH or acetone) in 500 mL capped round-bottom flasks. Ultrasonication was carried out in a sonic bath (Bandelin Sonorex, 100 W, 35 kHz). To maintain sonication efficiency and prevent overheating, the flask was kept in an ice-water bath. After being subjected to 48 h sonication, the samples were left to stand overnight to allow any unstable graphite aggregates to form and then centrifuged at 2000 rpm for 30 min. After centrifugation, the top two-thirds of the dispersion was gently extracted by pipetting. The graphene concentration (C_G) was determined by measuring the mass of the remaining solid after removal of the solvent by evaporation per volume of the dispersion. The dispersion was then diluted to 0.05 mg mL^{-1} for further use. To ensure validity in comparison regarding stability and Raman measurements, the G/i-PrOH dispersion was subjected to tip sonication with similar parameters as those applied during the synthesis of Ag/G/i-PrOH.

2.3. Deposition of Ag NPs on graphene

Typically, 20 mL of a graphene dispersion (C_G = 0.05 mg mL^{-1}) in i-PrOH or acetone was first subjected to 2 min tip sonication (Bandelin Sonoplus HD3100, 100 W, 20 kHz, 3 mm diameter tip). Subsequently, 1 mL of $AgNO_3$ and 1 mL of $NaBH_4$, both dissolved in a mixing solvent (90 vol% of the low-boiling point solvent and 10 vol% of distilled water), in turn were added dropwise into the dispersion, respectively, under tip sonication within 2 min in each case. The mass concentration of $NaBH_4$ was 5 times higher than that of the precursor. All synthetic processes were conducted at room temperature. The ultrasonic power (P) was estimated by calorimetric measurements using the equation $P = mC_{H_2O}\Delta T/t$, where m is the mass of water, C_{H_2O} is the heat capacity of water (4.18 J g^{-1} K^{-1}), ΔT corresponds to the resulting temperature rise, and t represents sonication time. The ultrasonic intensity (W cm^{-2}) was calculated from the ultrasonic power divided by the surface area of the tip (πr^2).

2.4. Investigation of NLO properties

To test the NLO response, the Ag/G composites were dispersed in i-PrOH at a concentration of 0.12 g L^{-1} followed by 30 min ultrasonic processing. The NLO properties of the samples were studied by using the open aperture Z-scan technique, which is widely adopted to investigate the nonlinear absorption, scattering and refraction processes. The Z-scan technique measures the total transmittance through the sample as a function of incident laser intensity, while the sample is gradually moved through the focus of a lens along the z-axis. In our work, the Z-scan was performed by

employing a Q-switched Nd:YAG laser of 6 ns pulses at a wavelength of 532 nm with a repetition rate of 10 Hz. The laser beam was tightly focused with a 10 cm focus lens, and all of the samples were examined in 0.1 cm quartz cells. The starting transmission of the dispersions was 50%.

3. Results and discussion

To colloidally stabilize graphene is key for a solvent to efficiently disperse it. For both carbon nanotube and graphene dispersions in solvents, dispersion quality was reported to be significantly related to the dispersive Hansen parameter, δ_D [8,20,21]. Successful graphene dispersions were only achieved for solvents matching 15 $MPa^{1/2} < \delta_D < 21$ $MPa^{1/2}$ [8]. Unfortunately, the δ_D values of low-boiling point solvents, such as i-PrOH (δ_D: 15.8), are at the very edge of the allowed range, leading to their poor stabilizing capabilities for graphene. Measuring the absorbance at 660 nm per unit cell length, A_{660}/l, versus sedimentation time allows one to monitor the dispersion stability in a quantitative manner [11]. Fig. 1 a shows A_{660}/l as a function of time for dispersions of G/i-PrOH, 1 wt%-, 3 wt%-, and (5 wt% Ag/G)/i-PrOH. A rapid decay in A_{660}/l by 40% took place for G/i-PrOH after 24 h, suggesting occurrence of severe aggregation/sedimentation of graphene. Fitting the data in the sedimentation time regime 0–24 h using an exponential approximation by $A_{660}/l = (A_{660}/l)_0 + [(A_{660}/l)_T - (A_{660}/l)_0]e^{-t/\tau}$ gave $(A_{660}/l)_0 = 116.92$, and $\tau = 19.82$ h. $(A_{660}/l)_T$ and $(A_{660}/l)_0$ correspond to the A_{660}/l of the initial dispersion and the stable phase, respectively, and τ is sedimentation time constant. This indicates that only 47% of the graphene in i-PrOH remained dynamically stable over 20 h, which is a relatively short period of time. Nevertheless, a two-phase exponential decay was found to fit well to all data sets (dashed line in Fig. S1a). A drastic decrease by 75% in A_{660}/l after 880 h was witnessed, indicative of strong degradation in dispersion quality. In sharp contrast, the dispersion of (1 wt% Ag/G)/i-PrOH retained very high stability without loss of A_{660}/l after 880 h. In the case of (3 wt% Ag/G)/i-PrOH, the absorbance remained constant up to 140 h, albeit with some decrease by 35% after 880 h. These results show clearly that decoration of graphene with small amounts of Ag NPs greatly enhances the stability of the graphene dispersions in i-PrOH. Similar effects were also observed for the dispersions in acetone. The dispersion of (1 wt% Ag/G)/i-PrOH was stable, showing no signs of settling after subjected to heating at 80 °C up to 24 h. Moreover, even after thermally treated at 150 °C (much higher than the boiling point of i-PrOH) for 2 h, the system remained uniformly dispersed without sedimentation or flocculation. This is in contrast to the formation of graphene hydrogel upon heating the aqueous dispersion of graphene oxide [22]. We are also surprised to find that the absorbance remained almost constant over 24 h before falling slightly for the dispersion of (1 wt% Ag/G)/i-PrOH diluted by water up to a 50% volume ratio (Fig. S1b). These observations are relevant for the practical handling of graphene-based dispersions.

The ability of Ag NPs to stabilize graphene depends critically on the particle size, distribution density, and loading content. Decreasing the particle diameter resulted in higher stabilizing capability at a given Ag loading, as illustrated in Fig. 1a. Although the enhancement in stability declined with increasing particle loading, the effect of stabilization was found to predominate the gravitational force in the regime <10 wt% Ag loading. It has been envisioned that individual graphene sheets dispersed in a solvent can move and rotate freely due to their kinetic energy. Once two sheets overcome the energy barrier and collide in a small area, very strong van der Waals forces (over 4650 kJ mol^{-1}) will drive them to recombine instantly. The occurrence of aggregation is therefore proposed to be a diffusion-controlled process [23]. We consider that Ag NPs inhibited the diffusion of graphene sheets, resulting in a smaller collision rate and consequently a slower aggregation rate. Furthermore, the restacking of graphene was impeded presumably due to steric hindrance and Coulomb interactions between the Ag NPs. On the other hand, decoration of graphene with Ag NPs, preferably on the edges, hindered the contact conformations of graphene sheets and the in-plane rotation, hence partly preventing the sliding assembly of graphene. Additionally, introduction of the NPs probably altered the atomic arrangement of the

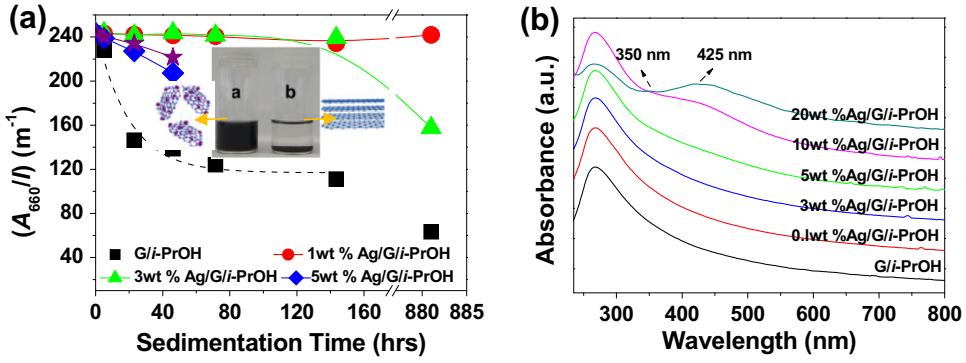

Fig. 1 – (a) A_{660}/l versus sedimentation time for dispersions of G/i-PrOH and Ag/G/i-PrOH at varying Ag loading levels. The pentagon symbol in the graph stands for (3 wt% Ag/G)/i-PrOH with a larger particle size. The dashed line is the fit to those data in the range 0–24 h for the G/i-PrOH. The solid lines are drawn to guide the eye. The inset shows photographs of (1 wt% Ag/G)/i-PrOH (a) and G/i-PrOH (b) after 40 days. (b) UV–visible spectra of G/i-PrOH and Ag/G/i-PrOH with Ag loadings ranging from 0.1 to 20 wt%.

solvent along graphene, thereby shifting the adsorption equilibrium toward a more steady state. Among others, the interaction between the NPs and graphene can cause increase in energy barrier enabling stabilization of individual graphene sheets. Not surprisingly, after removal of the solvent by evaporation, the solid obtained from the dispersion of (1 wt% Ag/G)/i-PrOH is more easily re-dispersed in i-PrOH via mild bath sonication without occurrence of aggregation of NPs (see Supporting Information) in comparison with the precipitate that resulted from G/i-PrOH.

As can be seen from the UV–vis spectra for the dispersions of G/i-PrOH and Ag/G/i–PrOH (Fig. 1b), a surface plasmon resonance absorption typical of Ag NPs appeared at ~425 nm (i.e., 2.92 eV) for (20 wt% Ag/G)/i-PrOH. Unexpectedly, the particle size estimated from the full width at half maximum (FWHM, ≈120 nm) of the absorption band using Mie theory is <4 nm being much smaller than 6.5 nm obtained by TEM [24]. This points to the influence of the absorption and scattering of graphene, leading to an increase in FWHM and thus decrease in particle size derived by Mie calculation. A weak absorption around 350 nm (i.e., 3.54 eV) was observed as well which may indicate the existence of Ag clusters in the sample as corroborated by TEM (vide infra) [25]. The main absorption attributed to the Ag clusters may be superimposed on the absorption from large Ag NPs in the wavelength range of 400–500 nm. However, no such peaks were observable for the Ag/G/i-PrOH with Ag loading levels below 5 wt%, probably due to the predominant interference from graphene. The strong peak shown at ~265 nm in all cases arises from the π-plasmon resonance commonly observed in graphitic materials [11]. We also found that there occurred a slight blueshift (≈3 nm) of the peak for the Ag/G/i-PrOH at 20 wt% Ag loading.

Fig. 2 shows the representative XRD patterns of the starting graphite and of 3 wt% Ag/G. The diffraction peaks at ~26.6° and 54.2° shown in traces A and B in Fig. 2 originate from the (002) and (004) reflections of the graphitic structure, respectively [26]. Both peaks in trace A appeared almost at the same positions as those in trace B, suggesting that the graphite lattice parameters were retained after exfoliation. However, in trace B, weakening of the relative intensity of the (004) peak occurred, and no (006) reflection was observed. This is in accordance with sublattices consisting of fewer

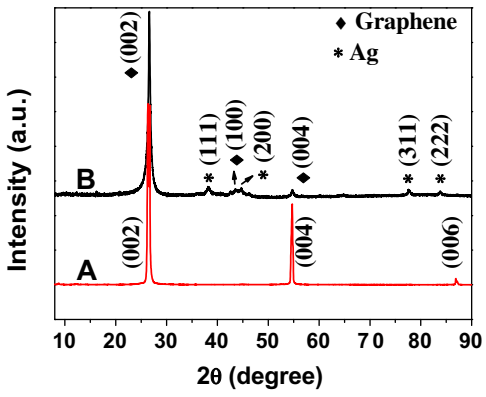

Fig. 2 – XRD patterns of pristine graphite (trace A) and 3 wt% Ag/G (trace B).

than four graphene layers [26]. A broad peak at 43.5° that is not present in trace A can also be seen, corresponding to the (100) plane of graphene, whereas no peak characteristic of graphene oxide at 10° was found, indicating the high quality of graphene without oxidation. The peak around 38.2° can be assigned to the (111) reflection of the Ag face-centered cubic (*fcc*) phase. The additional peaks appearing at 44.3°, 77.5°, and 81.6° are indexed as the (200), (311) and (222) planes of Ag. The unit-cell parameter α was calculated to be 4.079 Å, which agrees well with the value of 4.0862 Å for pure Ag (JCPDS file 4-783). The average crystallite size was estimated as 8.4 nm from the (111) reflection utilizing Scherrer's equation relating the coherently scattering domains with Bragg peak widths: $L = k\lambda/B\cos(\theta)$, where $k = 0.89$ for spherical particles and B is the full angular width at half-maximum of the peak in radians.

The nature of surface species in the as-obtained Ag/G was probed by X-ray photoelectron spectroscopy (XPS). The wide survey, O 1s, and C 1s spectra for the initial graphite, graphene and 3 wt% Ag/G are shown in Fig. S2 and Fig. 3a and b, respectively. Although deconvolution of the O 1s spectrum manifested three peaks at 530.7, 532.1, 533.5 eV indicating the presence of various oxygen-containing functional groups with doubly and singly bound oxygen, the atomic concentrations of oxygen in graphene and Ag/G were 3.2% and 3.4%, respectively. These values are of similar magnitude with that of 2% for pristine graphite, indicative of a very low level of oxidation of graphene during the exfoliation process. To gain more insight into the makeup of the exfoliated graphene, we studied the plasmon satellites occurring approximately from 5.6 to 7.2 eV above the main line of carbon (Fig. 3b). These structures are closely associated with the π–π^* and 2p–π interactions and also interfere with the oxidized C–O functional groups. A decrease in intensity was observed for the Ag/G sample, which was further confirmed by subtracting the spectrum from pristine graphite (Fig. 3c). The depletion in the region suggested a loss in graphite stacking order after deposition of the Ag NPs, consistent with the random orientation of graphene sheets. The two peaks at both sides of the C–C binding energy result from the slight broadening of the main carbon signal in the samples of G and Ag/G relative to the pristine graphite, which relates to the generation of defects induced probably by sonication-cutting effect. The Ag $3d_{5/2}$ binding energy was centered at 368.4 eV, in line with previous report on Ag (0) (Fig. 3d) [27]. The other weaker doublet in the Ag 3d core level XPS indicates the presence of a small amount of oxidic Ag, which may originate from the slight oxidation of Ag NPs upon exposure of the product to ambient air.

Fig. 4a and b show optical and SEM images of a typical film formed by vacuum filtration of the (1 wt% Ag/G)/i-PrOH. Significant quantities of large flakes were visible in the optical image appearing as bright regions. SEM observations showed that there also existed many small flakes with lateral sizes of 300 nm–1.5 μm that lay flat on top of each other (Fig. 4b). The flake length is approximately 3 times as large as the flake width. The presence of Ag in the NPs was confirmed by EDX (Fig. S3) together with elemental mapping (Fig. 4c and d). No large NP aggregates or agglomerates were observed during SEM imaging of the sample. The edge of the film showed a layered morphology (Fig. S4), the roughness of which may

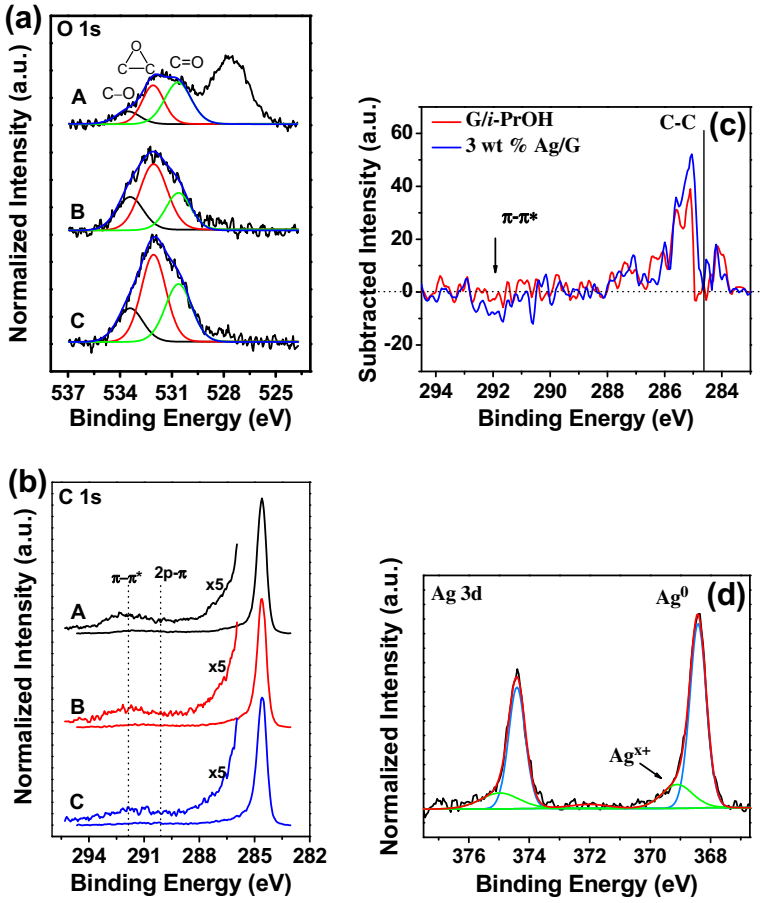

Fig. 3 – (a) O 1s, and (b) C1s XPS spectra of (A) graphite, (B) graphene powder after evaporation of the solvent i-PrOH and (C) 3 wt% Ag/G. (c) XPS spectra for the samples of G/i-PrOH and 3 wt% Ag/G after subtraction of the spectrum from pristine graphite. (d) Ag 3d XPS spectrum of 3 wt% Ag/G.

be attributed to the presence of Ag NPs. The NPs acted as spacers between adjacent graphene sheets inhibiting the direct stacking of graphene. This led to increase of their available surface areas when cast into films. For many applications, exfoliated graphene sheets need to be free of any stabilizer. One way to remove volatile stabilizing solvents while retaining the dispersed morphology is through freeze-drying. Low-boiling solvents such as i-PrOH and acetone are suitable for freeze-drying because of their high vapor pressures. Ag/G sponges with high microporosity were formed after removal of the solvent from the dispersion at low temperature. Such morphology probably arose from the assembly of sheets via edge-to-edge and edge-to-surface interactions (Fig. 5a) [28]. The three-dimensional structure consisting of misaligned and interconnecting flakes may have potential applications in catalysis and electronics.

TEM observations for 20 different sample areas showed that NPs with uniformity in diameter remained well dispersed on graphene (Figs. 5b and S5a). The NPs appeared to preferentially deposit on the edges as highlighted by arrows in Fig. S5a. This may be due to the fact that heterogeneous electron transfer occurs far more rapidly at the edges of a graphene sheet (a typical rate constant, k, is approximately 0.02 cm s^{-1}) than at basal planes ($k < 10^{-9}$ cm s^{-1}) [29]. Alternatively, small NPs tended to distribute on few-layer (<5) G. A relevant explanation is that a thin graphene sheet has a larger surface diffusion barrier (E_d) and lower diffusion coefficient ($D \propto \exp(-E_d/KT)$, K and T are Boltzmann constant and temperature, respectively) for Ag NPs than a thick one [30]. Some clusters of size $\leqslant$1.5 nm were also observed on graphene, and were found to be stable against electron beam-induced aggregation. A close TEM inspection of the sample offered evidence for a single Ag NP embedded in between two graphene sheets (inset of Fig. S5a). A selected area electron diffraction (SAED) pattern shows distinct concentric rings, characteristic of polycrystalline Ag (inset of Fig. 5b). Intense spots from a graphene-like lattice are clearly visible as well. The multiple spots are likely a superimposition of several hexagonal patterns from many individual graphene sheets [31]. This observation suggests that there are no preferred overlapping orientations between Ag-coated graphene flakes. On the basis of the TEM observation and by assuming that the NPs are spherical, the mean particle diameter for 100 different NPs (d_{mean}) at 1 wt% Ag loading amounts to 3.33 ± 0.13 nm, whereby the surface area and the number density of Ag were estimated to be 84.2 $m^2 g^{-1}$ and 4.98×10^{16} NPs per gram of graphene, respectively [32]. Further, based on the number density of Ag and graphene density (2000 kg m^{-3}), the number of particles per sheet was roughly calculated to be in the range of 40–400, provided the

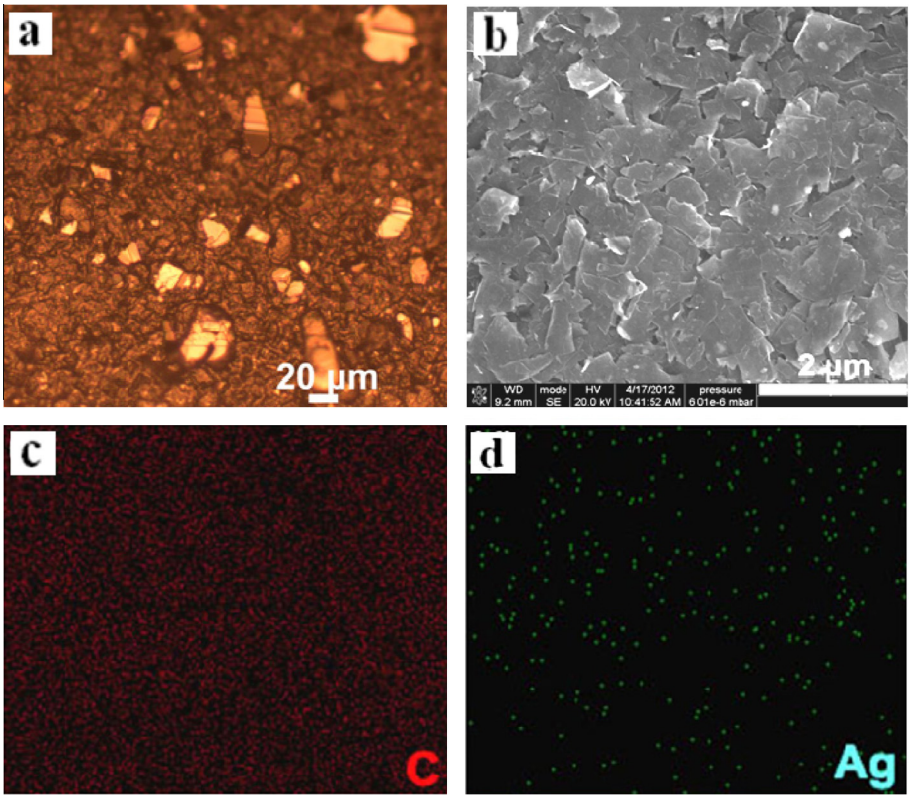

Fig. 4 – (a) Optical and (b) SEM images of the surface of a Ag coated graphene film formed by vacuum filtration of the (1 wt% Ag/G)/i-PrOH dispersion. EDX mapping data of (c) C and (d) Ag gleaned from the area shown in b.

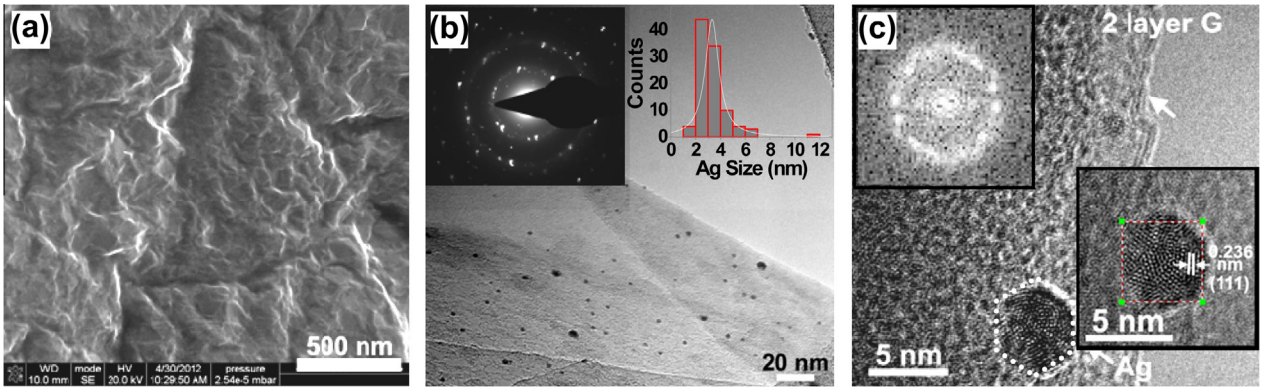

Fig. 5 – (a) SEM image of a three-dimensional structure formed by freeze-drying a suspension of (1 wt% Ag/G)/i-PrOH. (b) TEM image of 1 wt% Ag/G. Left inset: SAED pattern from the entire region shown in the inset of Fig. S3a. Right inset: Size distribution of Ag NPs. (c) HRTEM observation of an individual bilayer sheet decorated by Ag NPs. Top and bottom insets correspond to the FFT and enlarged HRTEM image of the NP shown in b, respectively.

ratio of flake length to width is 3 (mean flake length ≈595 nm estimated by Raman spectroscopy, Fig. 8) and the number of graphene layer is less than 10. This is in agreement with TEM observations (Fig. 5b). The surface average dispersion, D, was calculated to be 36.6% by the relation based on the Borodzinski and Bonarowska model: $D = 2.64/(d_{mean}/d_{at})^{0.81}$, using the atomic diameter, d_{at}, of Ag (2.88 Å) [33]. Fig. 5c is a HRTEM image of an individual bilayer sheet decorated with Ag NPs. The lattice spacing of the NP was measured to be 0.236 nm, corresponding to the (111) plane of the crystallite (bottom inset of Fig. 5c). The slightly distorted hexagonally shaped NP clearly indicates the preferred growth of the (111) plane of the cubic symmetry. The fast Fourier transform (FFT) of the lattice image suggests that the NP has a *fcc* structure (top inset of Fig. 5c). Fig. 6a shows a typical AFM image of Ag/G at 0.1 wt% Ag loading, in which the cross-section view on the left confirms the formation of monolayer graphene. Wrinkling of graphene sheets was observed as well, as displayed in Fig. 6b. In both images, Ag NPs, appearing as bright spots, are well distributed on the graphene surfaces. The sizes of particles are in the range of 1.5–3.5 nm, consistent with the TEM observations.

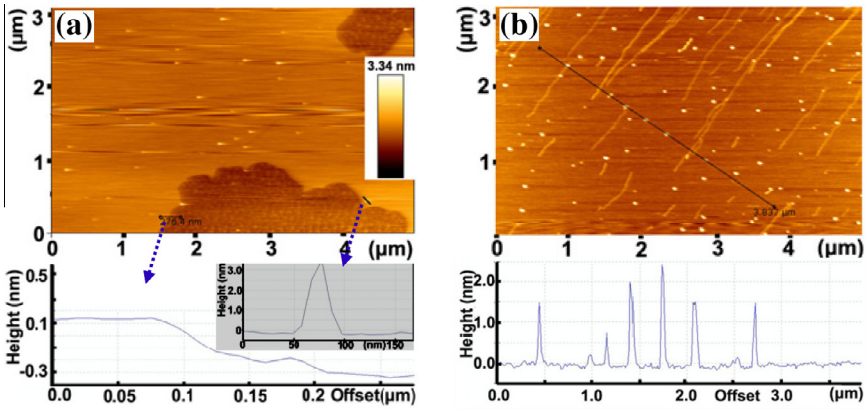

Fig. 6 – AFM images of Ag NPs deposited on G (a) without and (b) with wrinkles at 0.1 wt% Ag loading. The bottom patterns show their corresponding line sections.

The size of Ag NPs can be readily tailored by varying their loading level on graphene, ultrasonic intensity, precursor concentration, and feeding strategy. The size of the Ag NPs increases with the Ag loading at a given graphene concentration, and can be tuned in the range from 3.33 to 6.48 nm by increasing the Ag loading from 1 to 20 wt% (Fig. 7). In addition to some large crystallites, a number of very small NPs with size $\leqslant$2 nm were also found at a high Ag loading of 20 wt% (Fig. S5b and c). We plotted the Ag particle size as a function of the cube root of the Ag-to-G mass ratio, taken as $a^{1/3}$, as presented in Fig. S7. Note that the particle size is unlikely in a linear relation with $a^{1/3}$. This implies that the number of the NPs changed with the metal loading level, differing from the observation for Pt/MWCNT [32]. Moreover, the size of the NPs in the regime $a^{1/3} \geqslant 0.031$ was found to be significantly less than the value derived from the linear curve plotted from the $a^{1/3}$ at 1 wt% Ag loading, provided the NPs are spherical. Such behavior suggests that the number density of Ag tends to increase with increasing Ag loading, but the increase becomes slower at higher loading levels. By altering the precursor concentration while keeping the Ag loading fixed, the size of the Ag NPs was finely tuned. As a control experiment, the size of the Ag NPs was reduced from 6.16 to 4.21 nm at 3 wt% Ag loading by decreasing the concentration of $AgNO_3$ from 0.097 to 0.048 mg mL^{-1}. This scenario is due to the fact that lower amounts of Ag^+ contributed to the growth of nuclei at lower quantities of precursor addition. Alternatively, as the output ultrasonic intensity was increased from 15.79 ± 0.69 to 127.80 ± 1.14 W cm^{-2} while keeping the Ag loading at 10 wt% and its precursor concentration constant, the size of the Ag NPs decreased by 3% to 6.13 nm, as shown in Fig. 7. This decrease may be associated with the enhancement of nucleation rate as a result of more cavitation bubbles generated by the higher ultrasonic energy. On the other hand, manipulation of the adding way of NaBH4 enabled tuning of the particle size as well. For example, keeping both the precursor concentration and ultrasonic intensity constant, the particle size increased by 3.3% to 3.44 nm at 1 wt% Ag loading when $NaBH_4$ was added once rapidly. Finally, the particle size was tailored by employing a two-step feeding protocol, that is,

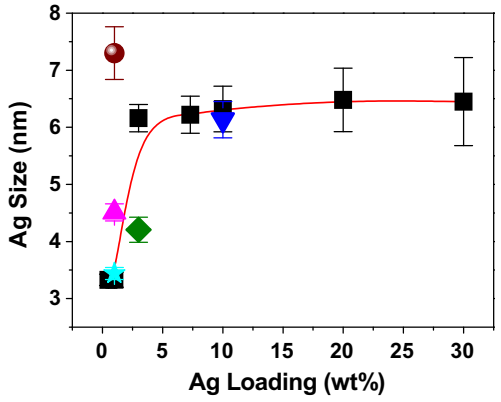

Fig. 7 – Ag particle size as a function of Ag mass loading on graphene (■) at a given ultrasonic intensity of 15.79 ± 0.69 W cm^{-2}. The ♦ and pentagon symbols stand for the particle sizes in cases of a half precursor concentration and addition of $NaBH_4$ once rapidly, respectively. The ▼ and ▲ symbols represent the sizes of the particles generated at ultrasonic intensity of 127.80 ± 1.14 W cm^{-2} and by a two-step feeding strategy, respectively. The ● symbol corresponds to the size of the particles prepared by applying magnetic stirring. The line is drawn to guide the eye.

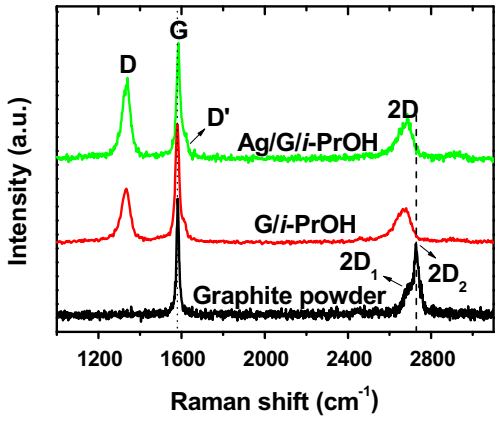

Fig. 8 – Raman spectra for the starting graphite powder and thin films prepared from dispersions of G/i-PrOH and (1 wt% Ag/G)/i-PrOH.

that half of the amount of precursor was first added and reduced followed by addition of the second half. In principle, the initial adding of $AgNO_3$ favored a rapid nucleation process generating monodispersed NPs according to the LaMer mechanism [34], while nucleus growth took place predominately upon addition of the precursor in the second step. Using such a strategy resulted in an increase in the particle size by 35% to 4.51 nm at 1 wt% Ag loading, as illustrated in Fig. 7 and S6b.

The application of ultrasonication results in unique advantages, particularly in the evolution of the small Ag NPs and their uniform deposition on graphene. Specifically, the mechanical effects of cavitation that include acoustic streaming, turbulent flow, microjets and emission of shock waves greatly promoted the mass transfer of reactants, permitting better wetting of the graphene surfaces with $AgNO_3$ solution. The reduction of Ag^+ by $NaBH_4$ was dramatically accelerated at ambient conditions by shock waves generated during cavitation with instantaneous temperatures up to 5000 K, pressures in excess of 20 MPa, and rapid heating/cooling rates $>10^9$ K s^{-1} [26]. From a sonocrystallization point of view, ultrasonic radiation can induce the primary nucleation at lower supersaturation levels and can also significantly reduce the induction time and metastable zone width. We roughly compared the time scale of crystallization taking place upon addition of $NaBH_4$ with that of mixing. In light of a mixing time of 111.5 s for a 0.006 m^3 vessel at an ultrasonic power density of 7 kW m^{-3} [35], the mixing time in our system (with a volume of 0.00002 m^3 and an ultrasonic power density of 55.8 kW m^{-3}) was estimated to be about 0.4 s for each aliquot of $NaBH_4$ solution (assuming a linear dependence of mixing time with volume). Actually, the mixing time is overestimated because the power density here exceeds the reported value. Given that the feeding rate of $NaBH_4$ was controlled at 2.5 s per aliquot, the time of crystallization is $\geqslant$5 times higher than that of mixing, guaranteeing a uniform crystallization process. Consequently, a sharp rise in nuclei population and rate of nucleation may have occurred, presumably as a result of the shock waves, resulting in small particle sizes. Alternatively, NP agglomeration was suppressed due to shortening in crystal contact time as well as increase in the number of collisions between the support and the Ag nuclei facilitated by ultrasound. In contrast, a large number of NP aggregates with nonuniformity in size were formed when magnetic stirring was applied instead under otherwise identical conditions (Figs. 7 and S6a). The average particle size and its standard error were 2.2 and 3.5 times, respectively, as high as those for the Ag NPs that were obtained via ultrasonication.

Raman spectra of the original graphite powder and thin films that were prepared from dispersions of G/i-PrOH and (1 wt% Ag/G)/i-PrOH are shown in Fig. 8. The Raman spectrum of G/i-PrOH displays three prominent peaks: a G band at about 1579 cm^{-1}, a second-order two phonon mode 2D (or G′) band at about 2670 cm^{-1}, and a disorder-related D peak at about 1337 cm^{-1}. The G band is typically assigned to the first-order scattering of the E_{2g} mode of C sp^2 atoms, whilst the D band is associated with the breathing mode of κ-point phonons of A_{1g} symmetry. An additional weak D' peak (~1616 cm^{-1}) appeared as a high-frequency shoulder to the G band, resulting from the Stokes scattering by a longitudinal optical phonon. Note that the 2D line with a single peak is characteristic of thin flakes that are composed of fewer than 5 graphene layers that are positioned one on top of the other in a random orientation [11,36]. The peak was significantly broadened compared to that of graphene grown by chemical-vapor deposition, which may be due to the small size of graphene produced here. This result was in contrast with the doublet 2D shape of graphite, which consists of two components $2D_1$ and $2D_2$ indicative of an unperturbed ABAB stacking sequence along the *c*-direction of the bulk material [36]. The exfoliation of graphene was also supported by the observation that a shift (about 68 cm^{-1}) to lower wavenumbers occurred for the 2D band of graphene as compared to graphite [11]. The intensity of the D band relative to the G band (I_D/I_G) was about 0.44, which compared better with graphene sheets that were produced from reduction of graphene oxide by hydrazine ($I_D/I_G \approx 1.44$) [37] or by sodium-hydride ($I_D/I_G \approx 1.08$) [38]. We suppose that the defect population may be dominated by edge defects from small graphene flakes that were obtained due to cavitation-induced scission effects. The in-plane crystallite size of graphene was determined to be approximately 38 nm using the equation $560(I_D/I_G)^{-1}/E^4$, where *E* is the laser energy (2.41 eV) [11]. A correlation of the D/G intensity ratio and flake length by *L* (nm) $\approx 260/(\Delta I_D/I_G)$ allowed for a rough estimation of the mean flake length to be 595 nm in G/i-PrOH [10], which agrees with TEM and SEM observations. The distance between defects, L_D, and the defect density in the basal plane, n_D, were calculated to be 17.02 nm and 1.08×10^{11} cm^{-2}, using the approximations of $L_D{}^2$ (nm^2) $= 4300(I_D/I_G)^{-1}/E^4$ and n_D (cm^{-2}) $= 7.3 \times 10^9 E^4(I_D/I_G)$, respectively [39]. These values essentially reflect the good quality of graphene. In the case of Ag/G/i-PrOH, the position of the G band shifts to a higher wavenumber (1583 cm^{-1}). This upshift may indicate phonon stiffening due to interaction between Ag and graphene via electron transfer driven by the work function difference [40], since the location of the G band is insensitive to the number of layer once the number of layers is more than 2 [41]. An increase in I_D/I_G was observed for Ag/G/i-PrOH ($I_D/I_G \approx 0.68$), which may be due to surface-enhanced Raman scattering, mainly attributed to the strong localized electromagnetic fields of Ag NPs. The intensity ratio of G to 2D band is 3.68 for Ag/G/i-PrOH, as compared to that of 3.59 for G/i-PrOH. The increase may be explained by the fact that the enhancement factor for the G band is much larger than that for the 2D band [40].

Ag-stabilized graphene dispersions can be used in a range of applications including the formation of conductive films. The film prepared from (1 wt% Ag/G)/i-PrOH (thickness: ≈5 μm) without annealing exhibited conductivity of 10,134 S m^{-1}, which is ~2.1 times as high as that of G/i-PrOH. The increase in conductivity results from the contributions of the attached Ag NPs in creating conducting pathways. We would expect a more remarkable increment in conductivity for films with higher Ag loadings. Alternatively, using Ag as a sacrificial template permitted the fabrication of bimetallic NPs (such as Ag-Pt) anchored on graphene through the galvanic metal exchange reaction assisted by ultrasound (Fig. S8).

As has been reported recently [42,43], pure graphene dispersions exhibit remarkable NLO response as a result of

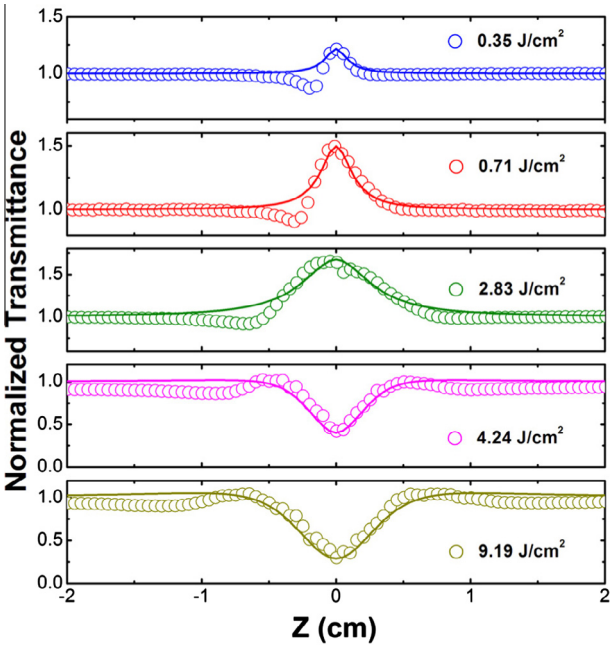

Fig. 9 – Open-aperture Z-scans of (1 wt% Ag/G)/i-PrOH at 532 nm with different incident laser energy densities. The solid lines are fitting results based on the propagation model shown in Eq. (1).

saturable absorption (SA) at low incident intensities and thermally induced nonlinear scattering (NLS) at high input energies. Ag NPs also have a strong NLO effect, which is attributed to two-photon absorption (TPA) as well as to free-carrier absorption (FCA). From these scenarios, we believe that a combination of the four different mechanisms for the NLO responses, i.e., NLS, TPA, FCA and SA enables the creation of a novel optical material with unique NLO features, which is indeed the case. Fig. 9 depicts the typical open aperture Z-scan curves of the (1 wt% Ag/G)/i-PrOH with nanosecond (ns) laser pulses at 532 nm performed at different incident laser energy densities. At low excitation energy density of 0.354 J cm^{-2}, the normalized transmittance was observed to decrease first and then increase as the sample was moved into the beam focus (z = 0), indicating a change from TPA/FCA to SA. The SA became much more pronounced when the incident energy density was increased to 2.83 J cm^{-2}. With further increasing the incident energy density, the value of the peak transmittance around the beam focus started to decrease. The maximum transmittance became less than 1, when the excitation energy density was enhanced to 4.24 J cm^{-2}. This means that the NLS effect exceeded the effect of SA under the high energy excitation. Further, the lowest normalized transmittance reached ~0.2 at higher excitation energy density of 9.19 J cm^{-2}.

It is clearly seen that the NLO response of Ag/G/i-PrOH for ns pulses at 532 nm results from a combination of TPA/FCA and SA at low excitation energy densities, and SA plays the major role, while TPA, SA and NLS have common influences on the NLO response at high excitation energy densities in which NLS dominates. On the basis of the NLO theory, the propagation equation in the dispersions can be expressed as:

Table 1 – Fitting parameters of the data shown in Fig. 9.

Energy density (J/cm^2)	β (cm/GW)	I_s (GW/cm^2)
0.35	0	0.9
0.71	0	0.3
2.83	0	0.41
4.24	16	0.3
9.19	13	0.28

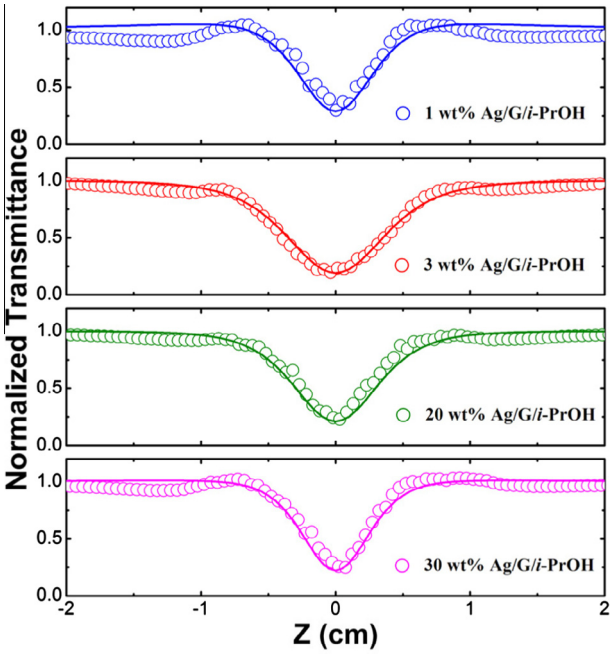

Fig. 10 – Open-aperture Z-scans of the Ag/G/i-PrOH with varying Ag loading levels at 532 nm with incident laser energy density of 9.19 J cm^{-2}. The solid lines are the fitting results using the propagation equation, Eq. (1).

$$\frac{dI}{dz'} = -\alpha(I)I \tag{1}$$

where I denotes the excitation intensity and z′ corresponds to the propagation distance in the sample. The total absorption $\alpha(I)$ can be expressed as:

$$\alpha(I) = \frac{\alpha_0}{1 + I/I_s} + \beta I \tag{2}$$

where I_s is the saturation intensity and β is the nonlinear extinction coefficient. The term, $\frac{\alpha_0}{1+I/I_s}$, in Eq. (2) stands for SA, whilst the term, βI, represents a combined effect of NLS, TPA and FCA. Fitting the data using this model, as illustrated in Fig. 9, agrees well with experimental results. The corresponding fitting parameters are summarized in Table 1. Note that the composites show a significantly larger nonlinear extinction coefficient and lower saturation intensity in comparison with other nanomaterials, such as single-walled carbon nanotubes, graphene and their derivatives [42,12]. The versatile NLO properties suggest that the Ag/G composites have a large potential in nanophotonic applications, such as optical limiting, optical switching and saturable absorbers.

Table 2 – Fitting parameters of the data shown in Fig. 10.

Sample	β (cm/GW)	I_s (GW/cm^2)
(1 wt% Ag/G)/i-PrOH	13	0.28
(3 wt% Ag/G)/i-PrOH	22	0.30
(20 wt% Ag/G)/i-PrOH	18	0.35
(30 wt% Ag/G)/i-PrOH	14	0.37

The Ag/G composites at varying Ag loadings display a similar NLO behavior with the increase in the incident energy density, as shown in Fig. 9. As an example, Fig. 10 displays the open aperture Z-scan results of the Ag/G/i-PrOH samples with different Ag loadings at an excitation energy density of 9.19 J cm^{-2}. For all composites, a slight SA followed by a significant NLS-induced optical limiting was observed, and the lowest normalized transmittance remained almost constant at ~0.2. This further confirmed that the optical limiting mainly originates from graphene. As shown in Fig. 10, the results derived from the propagation model based on Eqs. (1) and (2) fit the experimental data well. The corresponding fitting parameters are summarized in Table 2.

4. Conclusions

Highly stable graphene dispersions in low boiling point solvents were achieved by the uniform deposition of Ag NPs on the surface of graphene. Controlling the synthesis parameters such as ultrasonic intensity, feeding strategy, loading content and precursor concentration enabled the fine tuning of the particle size and, in this way, of the stabilizing effects of the NPs on the dispersions. The low boiling temperature and facile removal nature of the solvent improved the formation of conductive films and of three-dimensional structures with high microporosities through freeze-drying. The as-obtained Ag/G/i-PrOH dispersions showed versatile nonlinear optical properties at different excitation energy densities, which are required for nanophotonic applications such as absorber for ultrafast lasers and eye protection.

Acknowledgments

Zhenyu Sun thanks the Alexander von Humboldt Foundation for an experienced researcher fellowship. Jun Wang thanks the 100-Talent Program of Chinese Academy of Sciences, the National Natural Science Foundation of China (No. 61178007), and Science and Technology Commission of Shanghai Municipality (STCSM Nano Project No. 11nm0502400, Pujiang Talent Program 12PJ1409400). Ningning Dong gratefully acknowledges financial support from the China Postdoctoral Science Foundation (2012M520049).

Appendix A. Supplementary data

Supplementary data associated with this article can be found, in the online version, at http://dx.doi.org/10.1016/j.carbon.2013.06.010.

REFERENCES

[1] Novoselov KS, Geim AK, Morozov SV, Jiang D, Zhang Y, Dubonos SV, et al. Electric field effect in atomically thin carbon films. Science 2004;306:666–9.
[2] Geim AK, Novoselov KS. The rise of graphene. Nat Mater 2007;6:183–91.
[3] Bolotin KI, Sikes KJ, Jiang Z, Klima M, Fudenberg G, Hone J, et al. Ultrahigh electron mobility in suspended graphene. Solid State Commun 2008;146:351–5.
[4] Morozov SV, Novoselov KS, Katsnelson MI, Schedin F, Elias DC, Jaszczak JA. Giant intrinsic carrier mobilities in graphene and its bilayer. Phys Rev Lett 2008:100.
[5] Nair RR, Blake P, Grigorenko AN, Novoselov KS, Booth TJ, Stauber T, et al. Fine structure constant defines visual transparency of graphene. Science 2008;320. 1308–8.
[6] Hernandez Y, Nicolosi V, Lotya M, Blighe FM, Sun ZY, De S, et al. High-yield production of graphene by liquid-phase exfoliation of graphite. Nat Nanotechnol 2008;3:563–8.
[7] Lotya M, Hernandez Y, King PJ, Smith RJ, Nicolosi V, Karlsson LS, et al. Liquid phase production of graphene by exfoliation of graphite in surfactant/water solutions. J Am Chem Soc 2009;131:3611–20.
[8] Hernandez Y, Lotya M, Rickard D, Bergin SD, Coleman JN. Measurement of multicomponent solubility parameters for graphene facilitates solvent discovery. Langmuir 2010;26:3208–13.
[9] Khan U, O'Neill A, Lotya M, De S, Coleman JN. High-concentration solvent exfoliation of graphene. Small 2010;6:864–71.
[10] O'Neill A, Khan U, Nirmalraj PN, Boland J, Coleman JN. Graphene dispersion and exfoliation in low boiling point solvents. J Phys Chem C 2011;115:5422–8.
[11] Sun ZY, Masa J, Liu ZM, Schuhmann W, Muhler M. Highly concentrated aqueous dispersions of graphene exfoliated by sodium taurodeoxycholate: dispersion behavior and potential application as a catalyst support for the oxygen-reduction reaction. Chem Eur J 2012;18:6972–8.
[12] Wang J, Hernandez Y, Lotya M, Coleman JN, Blau WJ. Broadband nonlinear optical response of graphene dispersions. Adv Mater 2009;21:2430–5.
[13] Bonaccorso F, Sun Z, Hasan T, Ferrari AC. Graphene photonics and optoelectronics. Nat Photonics 2010;4:611–22.
[14] Zhao BS, Cao BB, Zhou WL, Li D, Zhao W. Nonlinear optical transmission of nanographene and its composites. J Phys Chem C 2010;114:12517–23.
[15] Lim GK, Chen ZL, Clark J, Goh RGS, Ng WH, Tan HW, et al. Giant broadband nonlinear optical absorption response in dispersed graphene single sheets. Nat Photonics 2011;5:554–60.
[16] Wang J, Chen Y, Li RH, Dong HX, Ju YF, He J, et al. Graphene and carbon nanotube polymer composites for laser protection. J Inorg Organomet Polym Mater 2011;21:736–46.
[17] Wang F, Zhang YB, Tian CS, Girit C, Zettl A, Crommie M, et al. Gate-variable optical transitions in graphene. Science 2008;320:206–9.
[18] Loh KP, Bao QL, Eda G, Chhowalla M. Graphene oxide as a chemically tunable platform for optical applications. Nat Chem 2010;2:1015–24.
[19] Kalanoor BS, Bisht PB, Ali SA, Baby TT, Ramaprabhu S. Optical nonlinearity of silver-decorated graphene. J Opt Soc Am B-Opt Phys 2012;29:669–75.
[20] Bergin SD, Sun ZY, Rickard D, Streich PV, Hamilton JP, Coleman JN. Multicomponent solubility parameters for single-walled carbon nanotube-solvent mixtures. ACS Nano 2009;3:2340–50.

[21] Bergin SD, Sun ZY, Streich P, Hamilton J, Coleman JN. New solvents for nanotubes: approaching the dispersibility of surfactants. J Phys Chem C 2010;114:231–7.
[22] Xu YX, Sheng KX, Li C, Shi GQ. Self-assembled graphene hydrogel via a one-step hydrothermal process. ACS Nano 2010;4:4324–30.
[23] Shih CJ, Lin SC, Strano MS, Blankschtein D. Understanding the stabilization of liquid-phase-exfoliated graphene in polar solvents: molecular dynamics simulations and kinetic theory of colloid aggregation. J Am Chem Soc 2010;132:14638–48.
[24] Baset S, Akbari H, Zeynali H, Shafie M. Dig J Nanomater Bios 2011;6:709–16.
[25] Genzel L, Martin TP, Kreibig U. Dielectric function and plasma resonances of small metal particles. Z Phys B-Condens Mat 1975;21:339–46.
[26] Shih CJ, Vijayaraghavan A, Krishnan R, Sharma R, Han JH, Ham MH, et al. Bi- and trilayer graphene solutions. Nat Nanotechnol 2011;6:439–45.
[27] He Y, Cui H. Synthesis of highly chemiluminescent graphene oxide/silver nanoparticle nano-composites and their analytical applications. J Mater Chem 2012;22: 9086–91.
[28] Oyer AJ, Carrillo JMY, Hire CC, Schniepp HC, Asandei AD, Dobrynin AV, et al. Stabilization of graphene sheets by a structured benzene/hexafluorobenzene mixed solvent. J Am Chem Soc 2012;134:5018–21.
[29] Ratinac KR, Yang WR, Gooding JJ, Thordarson P, Braet F. Graphene and related materials in electrochemical sensing. Electroanalysis 2011;23:803–26.
[30] Zhou HQ, Qiu CY, Yu F, Yang HC, Chen MJ, Hu LJ, et al. Thickness-dependent morphologies and surface-enhanced Raman scattering of Ag deposited on n-layer graphenes. J Phys Chem C 2011;115:11348–54.
[31] Wilson NR, Pandey PA, Beanland R, Young RJ, Kinloch IA, Gong L, et al. Graphene oxide: structural analysis and application as a highly transparent support for electron microscopy. ACS Nano 2009;3:2547–56.
[32] Sun ZY, Zhao YF, Xie Y, Tao RT, Zhang HY, Huang CL, et al. The solvent-free selective hydrogenation of nitrobenzene to aniline: an unexpected catalytic activity of ultrafine Pt nanoparticles deposited on carbon nanotubes. Green Chem 2010;12:1007–11.
[33] Borodzinski A, Bonarowska M. Relation between crystallite size and dispersion on supported metal catalysts. Langmuir 1997;13:5613–20.
[34] Lamer VK, Dinegar RH. Theory, production and mechanism of formation of monodispersed hydrosols. J Am Chem Soc 1950;72:4847–54.
[35] Kumar A, Kumaresan T, Pandit AB, Joshi JB. Characterization of flow phenomena induced by ultrasonic horn. Chem Eng Sci 2006;61:7410–20.
[36] Ferrari AC, Meyer JC, Scardaci V, Casiraghi C, Lazzeri M, Mauri F, et al. Raman spectrum of graphene and graphene layers. Phys Rev Lett 2006;97.
[37] Tung VC, Allen MJ, Yang Y, Kaner RB. High-throughput solution processing of large-scale graphene. Nat Nanotechnol 2009;4:25–9.
[38] Mohanty N, Nagaraja A, Armesto J, Berry V. High-throughput, ultrafast synthesis of solution-dispersed graphene via a facile hydride chemistry. Small 2010;6:226–31.
[39] Tomai T, Kawaguchi Y, Honma I. Nanographene production from platelet carbon nanofiber by supercritical fluid exfoliation. Appl Phys Lett 2012:100.
[40] Lee J, Novoselov KS, Shin HS. Interaction between metal and graphene: dependence on the layer number of graphene. ACS Nano 2011;5:608–12.
[41] Graf D, Molitor F, Ensslin K, Stampfer C, Jungen A, Hierold C, et al. Spatially resolved raman spectroscopy of single- and few-layer graphene. Nano Lett 2007;7:238–42.
[42] Wang J, Blau WJ. Inorganic and hybrid nanostructures for optical limiting. Appl Opt J Opt A-Pure 2009:11.
[43] Feng M, Zhan HB, Chen Y. Nonlinear optical and optical limiting properties of graphene families. Appl Phys Lett 2010:96.